

SEISMIC CHARACTERIZATION OF HYDRATES IN FAULTED, FINE-GRAINED SEDIMENTS OF KRISHNA-GODAVARI BASIN: PART I - UNIFIED IMAGING

P. Jaiswal^{1*}, P. Dewangan², T. Ramprasad² and C. A. Zelt³

* Email: priyank.jaiswal@okstate.edu, Phone: 405 744 6041, Fax: 405 334 7841

1. Boone Pickens School of Geology, Oklahoma State University, Stillwater, Oklahoma 74078, USA
2. Gas Hydrate Division, National Institute of Oceanography, Dona Paula, Goa 403 004, India
3. Department of Earth Science, Rice University, Houston, Texas 77005, USA

Abstract

A combination of diffusion and advection in fine grained sediments can create a patchy Bottom Simulating Reflector (BSR) which has little to no apparent correlation with the overlying hydrate distribution. Using 2D seismic data from faulted, clay-rich sediments in the Krishna-Godavari (KG) basin, we show both the hydrate distribution and the BSR structure are fault controlled. Our demonstration hinges upon a kinematically accurate P-wave velocity (V_P) model which is estimated using a composite traveltimes-inversion, depth-migration method in an iterative manner. The flexibility of the method allows simultaneous usage of traveltimes from multiple, discontinuous reflectors. The application begins with a simple V_P model from time processing which is reflective of a diffusive, continuous, hydrate and free-gas-bearing system. The method converges in three iterations yielding a final V_P model which is suggestive of a patchy distribution of hydrates and free gas possibly developing through a combined diffusive-advective system. The depth image corresponding to the final V_P model can be interpreted for faults that suggest ongoing tectonism. The BSR appears to be truncated at active faults zones. Both the final V_P model and the corresponding depth image can be reconciled with the hydrate distribution and BSR depth at logging/coring sites located ~250m away from the line by projecting the sites along the strike direction of the regional faults.

Keywords: KG Basin; Gas hydrate; faults; depth imaging; P-wave velocity

1. Introduction

In marine environments the geothermal gradient and seafloor depth define a zone of stability (gas hydrate stability zone; GHSZ), within which gas, mostly methane, exists with water in crystalline arrangements known as gas hydrates (Buffett, 2000). Growth habits of hydrate within the GHSZ are varied; in coarse-grain sediments, they can reside in pore-spaces, support the sediment framework as load-bearing grains, or bind the sediment grains as cement; in fine-grained sediments, they can create or occupy veins and fractures; on or near the seafloor they can form massive mounds (Kvenvolden, 1994; Max, 2003). As a solid, 1m^3 of hydrate can contain up to 164m^3 of methane at STP (Sloan and Koh, 2007), which is viewed as a potent greenhouse gas as well as a source of energy. Hydrates have been of interest to communities investigating climate change (Svensen *et al.*, 2004), energy resources (Collett, 2002), and seafloor stability (Rothwell *et al.*, 1998).

When buried below the base of the GHSZ, hydrates become unstable and dissociate from a solid to a gas (and water) phase; resulting in a strong impedance contrast and creating a seismic reflection known as the Bottom Simulating Reflector (BSR; Shipley *et al.*, 1979). BSRs are typically identified as reverse polarity features in a seismogram (compared to the seafloor reflection), cross-cutting the background stratigraphy (Bouriak *et al.*, 2003; Hyndman and Spence, 1992; Kopp, 2002). The term BSR is used because it is commonly observed that the base of the GHSZ tends to mimic the topography (Clennell *et al.*, 1999). However, in basins affected by structural deformation, local fluid and heat flow, and spatially variable sedimentation, e.g., Gulf of Mexico (Ding *et al.*, 2008) and Krishna-Godavari (Dewangan *et al.*, 2011), the BSR profile may not correspond to the seafloor topography (Chand *et al.*, 2008; Wood *et al.*, 2002). BSRs have been used as indicators of overlying hydrates, though studies suggest that free gas contributes to BSR amplitudes more than the hydrates themselves (Andreassen *et al.*, 2000; Laird and Morley, 2011; Ruan *et al.*, 2006).

Hydrates alter the acoustic properties of their host sediments: they increase the bulk moduli and decrease the bulk density (Chand *et al.*, 2004; Helgerud *et al.*, 1999; Hu *et al.*, 2010; Yun *et al.*, 2007). However, estimating hydrate distribution and saturation from the acoustic properties of sediments is a non-trivial task. Local variations in permeability, fracture density, temperature and chlorinity within the GHSZ can result in a patchy hydrate distribution (Müller *et al.*, 2007; Tinivella *et al.*, 2002; Trehu *et al.*, 2004; Zillmer *et al.*, 2005). Depending on their distribution within their host sediments (even for

similarly homogeneous distributions such as pore-filling versus cementing), the same hydrate saturation may yield vastly different rock properties (Helgerud *et al.*, 2000; Zhao *et al.*, 2005). Even so, qualitative analysis of the GHSZ through P- and S- wave velocity modeling and amplitude inversion is routinely done to get information on hydrate bearing zones such as their spatial extent and, in some cases, the hydrate saturation (Chen *et al.*, 2007; Dai *et al.*, 2008; DeAngelo *et al.*, 2010; Grevemeyer *et al.*, 2000; Singh and Minshull, 1994; Xia *et al.*, 2000). However, most modeling and inversion applications use the BSR, making GHSZ characterization a challenge at sites with a poorly developed BSR.

The most common way of characterizing the GHSZ is by building P-wave velocity (V_P) models using a stacking velocity analysis (SVA; Al-Yahya, 1989) of multichannel seismic (MCS) data to examine zones of elevated velocities (Haacke *et al.*, 2009; He *et al.*, 2009; Hornbach *et al.*, 2003; Inamori and Hato, 2004; Dewangan *et al.*, 2011). However, SVA has notable pitfalls with respect to GHSZ velocity estimations. First, SVA is like a moving average filter that cannot capture lateral changes in V_P at a resolution less than the hydrophone streamer length. Second, SVA makes hyperbolic reflection move-out assumptions (Yilmaz, 2001). In structurally deformed basins, non-horizontal stratigraphy may generate non-hyperbolic reflection trajectories which may be further distorted if V_P varies over short distances (less than the streamer length) due to, say, changing hydrate saturation. Furthermore, at the base of the GHSZ, conflicting dips between the background stratigraphy and the BSR may create multiple move-out paths making SVA prone to subjectivity and error.

Traveltime inversion, a model-based method of estimating V_P , is an objective alternative to SVA (Lailly and Sinoquet, 1996; Le Begat *et al.*, 2004) and serves the goal of this study – to characterize hydrates associated with a patchy BSR in faulted sediments. The key in our approach is combining traveltime inversion with pre-stack depth migration (PSDM) through a feedback mechanism for estimating V_P . This method, hereafter referred to as Unified Imaging (UI), is based on the coupled inversion – migration method introduced by Jaiswal and Zelt (2008) for 2D land MCS datasets. We show that with UI, a kinematically correct V_P model which delineates hydrate-bearing regions with a resolution of less than one-third of the streamer length can be generated using conventional surface-towed, narrow-aperture (offset = target depth) 2D marine MCS data. We emphasize that UI can be performed without using a BSR, which is particularly useful when the BSR is poorly developed or difficult to identify. We demonstrate the UI method with data from the Krishna-Godavari (KG) basin, Indian east coast. The choice of the study area is motivated by two reasons: a) a drill site in the KG basin

(NGHP-01-10) recovered large amounts of hydrates associated with faulted sediments and a patchy BSR; and b) the site provides a test of the model's capacity to handle spatial variability because the hydrate saturation decreases from ~20% by pore volume in NGHP-01-10 to less than ~2% by pore volume in a second drill site (NGHP-01-12) located 500 m southeast without any notable change in the reflectivity character within the GHSZ (Collett *et al.*, 2008).

2. Method

UI implements traveltimes inversion and PSDM in a cyclic manner, simultaneously constructing a velocity model and a depth image (Jaiswal and Zelt, 2008). The underlying principle of UI is that if a given velocity model is the “true” velocity model, PSDM and zero-offset reflection inversion will yield the same structural solution. Zero-offset inversion is defined here as the inversion of reflection arrival times corresponding to coincident source-receiver pairs (e.g., time picks in stacked data) for updating the reflection interfaces while keeping the velocity model fixed. The key in UI is to identify common events in three datasets – the PSDM image, the stack, and the shot gathers. The PSDM image provides the interface geometry, the stacked data provides its equivalent zero-offset structure in time and the shot gathers provide the corresponding wide-aperture arrival times. In this application, four events have been used. Due to its patchy nature, the BSR is not used in modeling (see Application section). A brief overview of UI is provided below and the reader is guided to the original paper for details.

UI is implemented in two stages; a reference velocity model and a reference depth image are estimated through conventional processing in the first stage and then improved cyclically in the second stage; a cycle refers to a single run of inversion followed by depth migration. Velocity updates are computed from inversion of the wide-aperture traveltimes while updates in horizon depths are computed from depth migration. The updated velocity model is used for depth migration as well as zero-offset inversion. Interface geometry in the wide-aperture inversion is an interpretation of the depth image from the previous cycle while the velocity model for depth migration is from the current cycle, thus creating a feed back mechanism. While solving the inverse problem, the horizons are modeled as floating reflectors (Zelt, 1999).

Velocity models in UI are assessed through a congruency test designed to estimate their proximity to the “true” velocity model. A dimensionless coefficient known as the congruency factor, j , determines the mismatch between a depth-migrated interface and its equivalent from zero-offset

inversion; both depth migration and zero-offset inversion use the velocity model, which is being tested. Uncertainties due to the limited frequency bandwidth and random noise in inversion and migration are accounted for while computing the congruency factor.

$$\mathbf{j} = \frac{1}{n} \sqrt{\sum_{i=1}^n \left(\frac{z_i^p - z_i^v}{\sigma_i} \right)^2} \quad (1)$$

In equation (1), z^p and z^v are the interpreted and inverted interfaces and n is the number of depth points at which the interfaces are compared. σ_i is the uncertainty assigned at the i^{th} node. A value of unity for \mathbf{j} implies that the structural discrepancies have been fit to the level of the interpretational uncertainties and the unified imaging is said to have converged at this point. Similarly, a value of \mathbf{j} greater than unity implies that the velocity model requires improvement and a value less than unity suggests that the data have been overfit. The inversion – migration cycles in the last stage are repeated until a value of unity is achieved for \mathbf{j} . In this paper three cycles were required.

The traveltimes inversion part of UI solves for two variables in this paper – the reflection arrival times of the seismic events and the reflection interface geometry. The traveltimes are first computed on a regular grid by solving the Eikonal equation using the finite-difference scheme of Vidale (1988) modified to account for large velocity gradients (Hole and Zelt, 1995). Raypaths, in accordance with Fermat's principle, are then determined by following the steepest gradient of the time field from a receiver to a source. The inverse modeling, which is non-linear in nature, is solved linearly with the help of an initial model which is iteratively updated based on the mismatch between the observed and the predicted traveltimes. The inverse modeling formulates an objective function which is the L_2 norm of a combination of data errors and model roughness (second-order partial derivative; Lees and Crosson, 1989) and minimizes it to compute the model updates. For a given observed data vector d_{obs} and predicted data vector d_{pre} , the objective function for constraining only the interfaces (zero-offset inversion) is:

$$E(z) = \delta d^T C_d^{-1} \delta d + \lambda [\delta z^T C_{z,h}^{-1} \delta z] \quad (2)$$

The objective function for simultaneously constraining velocities and interfaces is:

$$E(s, z) = \delta d^T C_d^{-1} \delta d + \lambda \left\{ \beta [\delta s^T C_{s,h}^{-1} \delta s + s_z \delta s^T C_{s,v}^{-1} \delta s] + (1 - \beta) [\delta z^T C_{z,h}^{-1} \delta z] \right\} \quad (3)$$

In equations (2), and (3), $\delta d = d_{pre} - d_{obs}$ constrains the data errors and $\delta s = s - s_0$ is the slowness perturbation vector being solved for; s_0 is the starting slowness vector, C_d is the data covariance matrix; covariance matrices $C_{s,h}$, and $C_{s,v}$ measure horizontal and vertical roughness of the slowness perturbation, respectively, λ is the overall trade-off parameter that controls the degree of data misfit and model roughness, and s_z determines the relative importance of maintaining vertical versus horizontal model smoothness. $\delta z = z_0 - z$ is the interface depth perturbation vector being solved for; z_0 is the starting interface vector and $C_{z,h}$ is the covariance matrix that measures the interface roughness. In equation (3), β determines the relative weights of slowness and interface regularizations. Regularization is implemented by scaling with the inverses of the data and model (slowness and interface depth) space covariance matrices in an attempt to obtain the smoothest model appropriate for the data errors (Zelt and Barton, 1998). Equation (2) is used when zero-offset traveltimes from the stacked data are inverted to constrain the interfaces only. Equation (3) is used when wide-aperture traveltimes from shot gathers are inverted to simultaneously constrain the velocity model and the interface depths.

The data misfit in traveltimes inversion is assessed using the normalized form of the misfit parameter, the chi-squared error (χ^2 ; Bevington, 1969) defined as follows:

$$\chi^2 = \sum_{i=1}^n \left(\frac{t_i^p - t_i^o}{u_i} \right)^2 \quad (4)$$

In equation (4), n is the total number of observed traveltimes, t_i^p and t_i^o are respectively the i^{th} observed and predicted traveltimes, and u is the pick uncertainty. Assuming the errors in the observed picks are uncorrelated and Gaussian in nature, a value of χ^2 equal to unity indicates that the observed traveltimes have been fit to within their assigned uncertainties and the inverse problem has converged to an acceptable solution (the final model). The depth migration part of UI is performed in the pre-stack common-offset domain and is based on Kirchhoff's integral (Schneider, 1978). Both traveltimes inversion and depth migration in this paper neglect the shear wave and assume the subsurface is isotropic.

3. Study Area

KG basin, along the eastern margin of India, formed as a result of rifting between Indian and Australia/Antarctica during Late Jurassic – Early Cretaceous (Powell *et al.*, 1988; Subrahmanyam and Chand, 2006). Hydrates have been inferred in the KG basin from exploration seismic datasets. The ground-truthing of hydrate deposits in the Indian continental margin occurred in 2006 through collaboration between the Indian National Gas Hydrate Program (NGHP) and the United States Geological Survey (USGS). An extensive drilling/coring operation known as the NGHP-01 expedition was executed to assess the hydrate potential of the Indian continental margin. During the expedition, which lasted over four months, 15 sites were visited in the KG basin (Collett *et al.*, 2008). Three drill sites, NGHP-01-10, 12, and 13 (Figure 1), are relevant to this paper. The sites are located along a linear NW-SE transect parallel to and ~250 m NW of the seismic line used in this paper (Figure 1). Preliminary seismic imaging suggested the area around all three sites is fault dominated and characterized by a patchy BSR (Collett *et al.* 2008).

During the NGHP-01 expedition, Site NGHP-01-10 was both cored and logged, Site NGHP-01-12 only cored, and Site NGHP-01-13 only logged. The presence of gas hydrates was confirmed at Site NGHP-01-10 and 12 by visual observations. Hydrate saturation estimated from depressurization of pressure cores at NGHP-01-10 and NGHP-01-12 is respectively estimated at 17.6 – 25.4 % and 2 % of the pore volume. Chloride in the pore water at Site NGHP-01-10 has a deviation of 398 – 634 mM from its background value of ~556 mM indicating hydrate formation and dissociation. In contrast, no significant variation in chlorine concentration is observed at NGHP-01-12, also suggesting that hydrates at Site NGHP-01-10 may not extend to Site NGHP-01-12. Site NGHP-01-13 was drilled 150m NW of NGHP-01-12. Wireline resistivity at site NGHP-01-13 was found to be low compared to NGHP-01-10 (Figure 1). However, due to the fairly high resistivity over the background, in this paper we assume site NGHP-01-13 has hydrates (Cook *et al.*, 2010); the saturation is unknown, however.

4. Application and Results

The 2D MCS data used in this paper were acquired in a NW–SE orientation (Figure 1). The profile is 7.5 km in length and has a nominal fold¹ of 60. Data were acquired using a 1000 cu. in. airgun with 12.5 m shot and receiver spacing. The recording streamer was 1.5 km in length with 120 channels. The

¹ Number of traces in a CDP gather.

shortest source – receiver offset was 75 m. Data were recorded with a 1 ms sample interval with high cut anti-alias filters set at 500 Hz. The record lengths are 4 s. The overall signal-to-noise ratio is high in the 8 – 120Hz range. The 2D profile is part of a larger dataset acquired by the Oil and Natural Gas Commission Ltd. (ONGCL), India, in 2002 for a regional survey of KG basin for oil/gas exploration.

4.1 Data Processing

The raw MCS data suffered from timing errors² as the first multiple did not occur at twice the arrival time for the seafloor. The required static correction was computed in a trial and error manner wherein the data were repeatedly shifted in time before stacking (see below). A bulk shift of 74 ms was found to position the seafloor at half the time of its multiple in the stack. All subsequent processing included this bulk shift. Typically in marine datasets, multiples are a serious concern. However, due to the seafloor depth (~1000 m) the seismic coda of our interest lies before the first multiple and therefore no processing was focused on multiple-removal.

The MCS data serve two purposes – first, to provide a reflectivity image through depth migration, and second, to provide direct estimates of V_P through traveltime inversion. As a result, the data were processed through two streams. For depth migration, the low frequency noise was first attenuated using a 20-80 Hz bandpass filter. Next, the effect of the bubble pulse from the airgun source was removed using deconvolution followed by frequency-wavenumber (F-K) filtering to remove the effect of high frequency instrument noise trends in the middle and far offsets. The processed data were sorted in the CMP domain and used for SVA. The processed data were simultaneously sorted in common-offset domain and evenly populated for PSDM.

Since the velocity models used for PSDM in UI build upon the fidelity of SVA, our strategy of SVA was not only to generate the “best” stack but also a corresponding velocity model that has minimum structure and is laterally smooth. Minimum structure ensures that the stacking velocity model contains only those features that are required by, as opposed to merely being consistent with, the data. The smoothness of the velocity model aids PSDM by improving its stability (Kiyashchenkoa *et al.*, 1995). We performed SVA in an iterative manner. Each iteration comprised velocity picking followed by normal and dip moveout (NMO and DMO respectively) corrections, followed by inverse NMO corrections and re-picking of the velocities. A conscious effort was made to keep the stacking velocity

² Error in recorded time as to when the source was set off.

model as simple as possible and least biased by the BSR, wherever present. The process was iterated until two subsequent stacking velocity models had minimal (<1%) difference. At this stage the data were stacked (Figure 2). Simultaneous processing for traveltimes inversion was kept to a minimum (only a 20-80 Hz bandpass filter) so as to preserve the arrival times of reflections as much as possible.

4.2 First PSDM and Interpretation

The stacking velocity model is converted to an interval velocity model (hereafter referred to as Vel0; Figure 3a) and used for PSDM. The migration aperture is set to ~1.5 km and a maximum frequency of 60 Hz is migrated. The resulting image is considered a preliminary depth image of the subsurface; it is hereafter referred to as Image0 (Figure 4a). Based on reflection characteristics, four common horizons R1, R2, R3, and R4 are interpreted in the stacked data (Figure 2b) and Image0 (Figure 4e). Horizon R1 is the seafloor. Horizons R2 and R3 are stratigraphic horizons that could represent debris-flow events. Horizon R4 lies immediately on top of a strong regionally continuous event that appears to have a reverse polarity (compared to the seafloor); this event could represent the top of a gas bearing formation. In the stacked data, 1320, 423, 813, and 1220 picks are made for R1 – R4 respectively; these picks are inverted as zero-offset reflections. Based on the dominant frequency and the random noise, uncertainties of 2-10 ms and 2-10 m were assigned to the time and depth interpretations of the horizons R1 – R4.

4.3 First Congruency Test and Picking

Using the initial velocity model, Vel0, the zero-offset reflections corresponding to R1 – R4 are inverted to constrain their respective interfaces in depth (Figure 4i); Vel0 is maintained stationary for the zero-offset inversion. Discrepancy between the inverted and the interpreted horizons ($j=1.42$; Figure 4i) indicates that Vel0 requires improvements. Using the inverted interfaces and Vel0, the wide-aperture traveltimes were simulated honoring the acquisition geometry for the 120 shots spaced evenly at 62.5 m across the profile and were used as a guide for traveltimes picking.

Wide-aperture reflections could be easily picked for events R1 and R2. However, for events R3 and R4, wide-aperture picking was not straightforward due to the faulted nature of the horizons. In the end, 12200, 2880, 21600, and 11520 picks were made for events R1– 4 respectively. Uncertainties of 2 – 10 ms were assigned to the picks to account for the dominant frequency, ambient noise, and picking errors. The wide-aperture picks comprise the dataset for traveltimes inversion in the last stage of UI.

4.4 Joint Inversion and PSDM

The last stage of UI improves the velocity model (Figure 3) and the corresponding depth image (Figure 4) in three cycles. At the end of three cycles UI is halted yielding the final velocity model, Vel3 (Figure 3d), and the final depth image, Image3 (Figure 4d). The overall congruency of near unity is obtained and at this stage ($j=1.06$; Figure 4l). The remaining misfit in the traveltimes can be due to picking uncertainties, ambient noise, and/or anisotropy that has not been accounted for in traveltime inversion as well as PSDM. In the end, a value of 1000 for λ_0 , 0.15 for s_z and 0.5 for β , determined in a trial-and-error manner, was found to be optimal for the joint inversion in all three cycles.

4.5 Model and Image Assessment

Updates in Vel0, illustrated as a difference plot between Vel0 and Vel3, are presented as velocity perturbations on Vel0 (Figure 5a). Most significant updates occur at model distances $\sim 2.4\text{km}$, 3.9km , and 4.5km ; velocity decreases from Vel0 to Vel3 by up to $\sim 10\%$. To assess the resolution of Vel3 we perturb Vel0 in a checkerboard pattern, simulate reflection traveltimes from R1 – R4, and attempt to recover the checkerboard pattern (Zelt, 1999). The checkerboard tests suggest that anomalies with at least $200\text{m} \times 100\text{m}$ dimension (less than one-third of the streamer length) and 10% strength can be reasonably recovered in between the seafloor and R4 (Figure 5b). The checkerboard test provides a general test of the features in Vel3 that can be reliably interpreted.

A qualitative assessment of Vel3 is done by post migrated data comparison (Figure 6). Updates in velocity translate to improvements in migration if it enhances the flatness of the migrated event in a CDP gather. Migrated gathers from two CDP locations, 640 and 800, in Image0 and Image3 corresponding to $\sim 1\%$ and $\sim 8\%$ velocity changes are compared. The flatness of events in Image3 is generally greater as compared to Image0 indicating that velocity updates from UI are appropriate.

5. Discussion

5.1 Composite Interpretation

The discontinuous nature of seismic horizons is indicative of a faulted stratigraphy (Figure 7a). In general, two sets of faults (A and B) and their conjugates can be identified along the profile (Figure 7b). The first, Set A, dips 85° SE with a NW dipping conjugate (A') and the second, Set B, has a more gentle

76° NW dip with a SE dipping conjugate (B'). Set A is dominant near the NW end of the mound (CDP 300 - 550) while set B is dominant at SE end of the mound CDP (650 – 950). Fault sets A and B have previously been mapped and reported by Riedel *et al.* (2010) who interpret a 3D seismic volume in the study area. In 3D Set-A is SW-NE and with a NNW-SSE conjugate set and Set-B is NNE-SSW with a NEE-SWW conjugate set (Riedel *et al.*, 2010). Figure 7b suggests that sediments between CMP 650 and 850 are dominated by Set B faults which were also observed in the sediment core at Site NGHP-01-10 (Collett *et al.*, 2008).

All velocity models (Figure 3) show a decrease in velocities below the BSR which is consistent with a theoretical likelihood of the presence of free gas. $V_p < \sim 1.4$ is generally representative of free-gas-bearing unconsolidated sediments (Gist 1994; Domenico 1977). Possible locations of free gas below the BSR along the profile could therefore be at model locations ~2.4 km and ~4.5 km (Figure 3d). Both locations are concurrent with faults (F1 and F4 respectively) that offset R4, previously interpreted as top of a gas rich horizon (Figure 7b).

5.2 The Hydrate - Free Gas System

A composite of Image3 (Figure 4d) and Vel3 (Figure 3d) provide insight into the hydrate – free gas system along the seismic line and their relation to the BSR (Figure 7). In Image3, the dome shape of R4 suggests tectonic uplift. The sediment package between R2 and seafloor forms a wedge (Figures 2 and 4) suggesting that the sedimentation is syn-tectonic in nature and the uplift is post R2 in age. A bathymetric mound at the crest of the anticline (CMP 550- 750; Figures 2 and 4) appears to be acting as a barrier to sedimentation beyond CMP 750. While the seafloor SE of the mound (CMP 750 – 900; Figure 4d) appears to have undergone a gravitational collapse, the stratigraphy NW of the mound (CMP 200 – 450; Figure 4d) lacks any indications of a widespread shear failure in terms of faults or fractures.

The BSR in the NW part of the line (CMP 200 – 450; Figure 7), associated with near-horizontal seafloor, is continuous in nature and indicates a diffusive system which could be controlled by both hydrate-recycling and a solubility-curve mechanism (Haacke *et al.*, 2007). The hydrate recycling can conceivably occur as hydrates are pushed out of GHSZ due to an ongoing sedimentation. High (>1.7 km/s) V_p above the BSR in Vel3 in this part of the line (Figure 7c) strongly indicates hydrates at the base of the GHSZ. A lack of a thick and continuous free gas zone (FGZ) below the GHSZ in Vel3 suggests a high upward diffusive fluid flux.

The BSR in the SW part of the line (CMP 450 – 850; Figure 7) is patchy. A closer inspection suggests that the cause of its patchiness is interruption from large and small scale faults (Figure 8a). For example, while F1 and F4 (Figure 7b) penetrate the entire sediment column and offset the stratigraphy up to 50m, others such as F'1 and F'2 (Figure 8a) are local and may even be of sub-seismic resolution. The observed BSR - fault relation can occur when a diffusive hydrate – free gas system (Figure 8b) evolves through simultaneous tectonic uplift and a non-uniform sedimentation (Figure 8c). The tectonic uplift shallows the seafloor reducing the overall thickness of the GHSZ. As a result, the hydrates that are pushed out of the GHSZ dissociate, increasing the methane concentration below its base. The tectonic uplift also leads to shear failure creating fault zones in brittle sediment. By the term “fault zones” we intend to imply regions with possibly bigger and better interconnected pores. The high permeability fault planes provide opportunities for a rapid, focused, advective flow that increases the overall heat flow as well as depletes methane-rich fluids from below the GHSZ. Shear motion can also pulverize sediments and create gouge zones which have finer grain size. Although gouge zones will have a restricted fluid flow, the finer grain size will increase the methane solubility (Gibbs-Thompson effect; Daigle and Dugan, 2011). In either case, a fault zone will have the tendency to perturb the base of the regional GHSZ making the BSR discontinuous at its edge. Thus, in presence of multiple fault zones, the BSR can get an overall patchy appearance.

Between CDPs 800 – 850, a patchy BSR is also associated with a thick FGZ (1.1 – 1.25 km depth) and an overlying zone of high V_P (> 2 km/s) and low reflectivity (blank zone; Figure 7c). Lee and Dillon (2001) demonstrated that seismic blanking can occur when hydrate saturation is proportional to porosity, i.e., hydrate saturation is higher in more porous media and vice versa. They argued that depending on the hydrates saturation relative to the porosity, reflection amplitudes from hydrate-bearing sediments can be lesser or greater than those from corresponding non-hydrate-bearing sediments. However, applicability of their rationale in our case requires a mechanism that can enable the fluid flow to overcome the permeability restrictions in the fine-grained sediments and become unrestricted. The sub-BSR stratigraphy between CDPs 800 and 900 is ruptured by numerous faults that can be extended into the blank zone in an interconnected, checkerboard pattern (Figure 7b). Faults can increase permeability and therefore the fluid flow but they can also scatter seismic energy and create low reflectivity zones even in absence of hydrates. However, if blanking was only due to faults, it would be associated with an overall decrease in V_P (Barton, 2007) which is in contrast to the observed increase in V_P at the blank zone (Figure 7c). Therefore, we interpret the blank zone to be due to a proportionate (or

uniform) hydrate precipitation which is most likely driven by methane-rich flow through the higher permeability faults.

Besides shear failure of sediments, hydraulic fracturing stemming from pore pressure buildup from hydrate occlusion also creates (and saturates) faults in fine grained sediments (Daigle and Dugan, 2010a). Hydraulic fracturing can originate at the base of the GHSZ or at pre-existing planes of weakness within the GHSZ depending on the permeability contrast, phase of the methane (free or dissolved) in the fluid and the flow rate (Daigle and Dugan, 2010b; Jain and Juanes, 2009). Thus, a combination of shear failure and hydraulic fracturing can promote localized fault networks. Higher permeability faults planes can eventually become hydrate saturated in fine grained sediments through diffusion (Bhatnagar *et al.*, 2007) creating patchy, hydrate-bearing zones that concurrently exist with an underlying patchy BSR. As a closely related point, if the advecting fluids within the faults are higher salinity/temperature the depth of hydrate precipitation will occur shallower within the GHSZ, and, in a limiting case, may even be pushed up to the seafloor (Wood *et al.*, 2008).

The evolution of a combined advective-diffusive hydrate – free gas system from a dominantly diffusive system, as suggested above, can have two significant consequences. First, it implies that hydrates can be simultaneously present in two states within the GHSZ – in pore spaces which is the original state of hydrates in a diffusive system and in fault zones which result from a later fault-driven, advective system; both states were found in the NGHP-01-10 core (Collett *et al.* 2008). Second, it implies hydrates distribution will mimic the fault patterns; if some of the faults are regionally extensive, hydrate character could be predictable at large spatial scales.

5.3 Site NGHP-01-10 – 13 projections

SVA results in a fairly uniform V_P spread within the hydrate stability zone (Vel0; Figure 3a). As the model evolves from Vel0 to Vel3 through UI, V_P within the stability zone compartmentalizes (Figure 3d). In general, V_P of soft marine sediments within 200 m of the seafloor ranges from 1.4 – 1.7 km/s. In this paper, we assume that V_P higher than 1.7 km/s is firm indication of hydrate bearing sediments in the KG Basin (Collett *et al.*, 2008). Consequently, sediments with less than 1.7 km/s within the GHSZ are either hydrate-free or have hydrate saturation that is below the sensitivity of reflection traveltimes. Thus, segregation between hydrate bearing sediment patches can occur at three possible zones in Vel3 – model distance 2.3 – 2.4 km, model distance 3.75 – 4.15 km, and model distance 4.4 - 4.5km (Figure

3d). Speculating one of the three zones to be reflective of the disconnected hydrates at sites NGHP-01-10 and 12, we project the sites on the seismic line.

To first order of approximation we assume the best projection will not only maintain the mutual site separation but also be consistent with hydrate character at the three sites. Projection on the first zone highlights a BSR depth 10m deeper than at Site NGHP-01-10 (green well trajectories; Figure 3e). The seafloor depth at Site NGHP-01-10 differs by ~2m from its projected location in the first zone. A difference of 10m in GHSZ thickness therefore implies a net lowering in the regional geothermal gradient making this projection less likely. Projection on the second zone associates site NGHP-01-12 with hydrate free sediments (blue well trajectories; Figure 3e) which is inconsistent with its elevated resistivity (Figure 1) also making this projection unlikely. Projection on to the third zones allows all three sites to be associated with hydrate bearing sediments, and also maintains the correct depth of BSR at Site NHGP-01-10 (red well trajectories; Figure 3e). Projection on to the third zone almost exactly follows the regional strike of F1 – 4 faults (Dewangan *et al.*, 2011) suggesting that hydrates maintain continuity along the strike direction of the regional faults.

5.4 General applicability of UI in hydrate detection

UI is preferable over conventional processing because it enables an efficient implementation of PSDM. In faulted stratigraphy, non-hyperbolic reflections are commonly encountered. These reflections cannot be honored adequately in conventional, CDP-based time imaging. PSDM circumvents these challenges by reverse propagating the seismic energy back to the scatter points and thus obtaining images of subsurface reflectors directly in depth (Garu and Lailly, 1993; Pasasa et al., 1998). However, critical to the success of PSDM is a migration velocity model that is smooth as well as kinematically correct (Black *et al.*, 1994). As the seismic trace can be decomposed into its constituent frequencies, the velocity model can be decomposed into its constituent wavenumbers. The more heterogeneous the geology is, the more rapidly the wavenumber content changes from one part of the velocity model to another. The smoothness attribute of a velocity model refers to the ease with which one group of wavenumbers transition to another without compromising the kinematic accuracy, i.e., maintaining the correct raypath. Sudden changes in wavenumbers within the velocity model being used for PSDM, such as sharp velocity changes across a fault, can lead to numerical instability in ray tracing, creating modeling artifacts (Versteeg, 1993). On the other hand, velocity smoothing, e.g., across a fault, may not

render the velocity model suitable for direct interpretation for small-scale geological features, but may create an accurate reflectivity image.

Migration velocity models estimated using SVA run the risk of having wavenumber distribution that is not reflective of the geology but rather manifestation of the numbers and temporal separation of the horizons being used in SVA. As a result, ad-hoc smoothing of SVA models to avoid the arbitrary focusing and defocusing during migration are common (Gray *et al.*, 2001). When BSR is used as a key horizon for SVA and it is patchy, the migration velocity model is even more susceptible to being subjective. V_P estimated using UI has the following advantages: first, the traveltime inversion component of UI is a model-based method that honors the physics of wave propagation better than SVA, thus yielding more realistic V_P estimates. Second, multiple horizons with limited continuity can be used for V_P modeling as long as reflections from the composite horizon are consistently picked in shot gathers. Thus, even if the BSR is patchy, other reflections can be used for velocity modeling. The corresponding depth images can ensure compatibility with expected stratigraphy. Third, the effect of noise on model resolution can be reduced by weighing the data appropriately. Fourth, ray coverage information can be used to exclude parts of model that are not fit for interpretation such as in Figures 3 and 4 where no interpretation is made below R4. In fact, even in presence of a continuous BSR, UI can provide a supplementary attribute for hydrate detection in the form of V_P estimates.

The key finding in this paper, that hydrates maintain continuity along fault strike direction, could not be made without the subtle updates in depth imaging that resulted from UI application. Figure 5a suggests that V_P at CMP 775 – 825 changed by ~8% as UI updated a conventionally estimated V_P model in three iterations. Figure 5c suggests that the corresponding change in the BSR depth is ~15m at the location where well NGHP-01-10 is projected. The update is most significant where the BSR is patchy and arguably so because conventional depth imaging fails to correctly estimate V_P in the presence of a patchy BSR. If the well projection were made on a conventionally processed depth image (Image0; Figure 4a), the mismatch in BSR depth between that in the NGHP-01-10 well and in the image would be the same at the first and the third projection. The correct location of BSR at the third projection could be only made through UI.

6. Conclusions

V_P estimate of hydrate-bearing sediments can be objectively obtained using UI which develops a structurally consistent velocity model and depth image by cyclic implementation of traveltime inversion and depth migration. In three cycles, UI improves the spatial resolution of a simple starting V_P model, Vel0, estimated by SVA. The final model, Vel3, has a resolution of at least 200m X 100m and better migrates the data as compared to Vel0.

Given the resolution obtained from UI, a more detailed examination of the region can be made. The final depth image, Image3, suggests that syn-tectonic sedimentation suppresses seafloor failure in the NW part of the seismic profile, maintaining a sub-horizontal seafloor and creating a continuous BSR. Lack of sedimentation in the SE part along with the tectonic uplift creates rugged seafloor topography. Two dominant sets of faults and their conjugates are identified along the line. An otherwise continuous BSR becomes patchy due to interruption from active fault zones. Even in the presence of a patchy BSR, elevated (>1.7 km/s) velocities in Vel3 allow first-order hydrate detection suggesting that V_P is a better hydrate proxy than BSR amplitudes in faulted sediments. Finally, the patchy distribution of hydrates in Vel3 can be appropriately reconciled with Sites NGHP-01-10 – 13 by projecting the sites along strike of regional fault F1 – 4 suggesting that hydrates maintain continuity along the strike direction of regional faults.

7. Acknowledgement

Funding for the study was provided by the US Department of Energy (Award No.: DE-FC26-06NT42960). Our sincere thanks to ONGCL (India) for providing the seismic data. A. V. Sathe and M. V. Lall provided valuable input for modeling. The corresponding author thanks the Director, National Institute of Oceanography (NIO) for supporting the study during his tenure as visiting scientist at NIO. Discussions with H. Daigle and B. Dugan improved our understanding of fractures in fine sediments. Comments from W.F. Waite, I. Pecher, and an anonymous reviewer brought this paper into its final shape.

8. References:

- Al-Yahya, K., 1989. Velocity analysis by iterative profile migration. *Geophysics* 54, 718-729.
- Andreassen, K., Mienert, J., Bryn, P., Singh, S.C., 2000. A double gas-hydrate related bottom simulating reflector at the Norwegian continental margin, in: Holder, G.D., Bishnoi, P.R. (Eds.), *Gas Hydrates: Challenges for the Future*, pp. 126-135.
- Clennell, M. B., Hovland, M., Booth, J.S., Henry, P., Winters, W.J., 1999. Formation of natural gas hydrates in marine sediments 1. Conceptual model of gas hydrate growth conditioned by host sediment properties. *Journal of Geophysical Research-Solid Earth* 104, 22985-23003.
- Barton, N., 2007, *Rock Quality, Seismic Velocity, Attenuation and Anisotropy*, Taylor & Francis, London.
- Bevington, P.R., 1969. *Data Reduction and Error Analysis for the Physical Sciences*. McGraw-Hill, New York.
- Bhatnagar, G., Chapman, W.G., Dickens, G.R., Dugan, B., Hirasaki, G.J., 2007. Generalization of gas hydrate distribution and saturation in marine sediments by scaling of thermodynamic and transport processes. *American Journal of Science* 307, 861-900.
- Black, R.A., Steeples, D.W., Miller, R.D., 1994. Migration of shallow seismic-reflection data. *Geophysics* 59, 402-410.
- Bohrmann, G., Greinert, J., Suess, E., Torres, M., 1998. Authigenic carbonates from the Cascadia subduction zone and their relation to gas hydrate stability. *Geology* 26, 647-650.
- Bouriak, S., Volkonskaia, A., Galaktionov, V., 2003. 'Split' strata-bounded gas hydrate BSR below deposits of the Storegga Slide and at the southern edge of the Voring Plateau. *Marine Geology* 195, 301-318.
- Buffett, B.A., 2000. Clathrate hydrates. *Annual Review of Earth and Planetary Sciences* 28, 477-507.
- Chand, S., Mienert, J., Andreassen, K., Knies, J., Plassen, L., Fotland, B., 2008. Gas hydrate stability zone modelling in areas of salt tectonics and pockmarks of the Barents Sea suggests an active hydrocarbon venting system. *Marine and Petroleum Geology* 25, 625-636.
- Chand, S., Minshull, T.A., Gei, D., Carcione, J.M., 2004. Elastic velocity models for gas-hydrate-bearing sediments - a comparison. *Geophysical Journal International* 159, 573-590.
- Chen, M.A.P., Riedel, M., Hyndman, R.D., Dosso, S.E., 2007. AVO inversion of BSRs in marine gas hydrate studies. *Geophysics* 72, C31-C43.
- Collett, T., Riedel, M., Cochran, J., Boswell, R., Presley, J., Kumar, P., Sathe, A., Sethi, A., Lall, M.V., Sibal, V., 2008. Expedition 01 Initial Reports, Indian National Gas Hydrate Program.
- Collett, T.S., 2002. Energy resource potential of natural gas hydrates. *Aapg Bulletin* 86, 1971-1992.

- Cook, A. E., B. I. Anderson, A. Malinverno, S. Mrozewski, and D. S. Goldberg (2010), Electrical anisotropy due to gas hydrate-filled fractures, *Geophysics*, 75(6), F173-F185.
- Dai, J.C., Snyder, F., Gillespie, D., Koesoemadinata, A., Dutta, N., 2008. Exploration for gas hydrates in the deepwater, northern Gulf of Mexico: Part I. A seismic approach based on geologic model, inversion, and rock physics principles. *Marine and Petroleum Geology* 25, 830-844.
- Daigle, H., Dugan, B., 2011. Capillary controls on methane hydrate distribution and fracturing in advective systems. *Geochemistry Geophysics Geosystems* 12, DOI: 10.1029/2010gc003392
- Daigle, H., Dugan, B., 2010a . Origin and evolution of fracture-hosted methane hydrate deposits. *Journal of Geophysical Research-Solid Earth* 115, DOI: 10.1029/2010jb007492
- Daigle, H., and B. Dugan., 2010b, Effects of multiphase methane supply on hydrate accumulation and fracture generation, *Geophys. Res. Lett.*, 37, DOI:10.1029/2010GL044970.
- DeAngelo, M.V., Sava, D.C., Hardage, B.A., Murray, P.E., 2010. Integrated 2D 4-C OBC analysis for estimating hydrate concentrations, Green Canyon, Gulf of Mexico. *Journal of Seismic Exploration* 19, 263-278.
- Dewangan, P., Sriram, G., T., R., Ramana, M.V., Jaiswal, P., 2011. Fault system and thermal regime in the vicinity of site NGHP-01-10, Krishna–Godavari basin. *Marine and Petroleum Geology*, *in press*.
- Ding, F., Spiess, V., Bruning, M., Fekete, N., Keil, H., Bohrmann, G., 2008. A conceptual model for hydrocarbon accumulation and seepage processes around Chapopote asphalt site, southern Gulf of Mexico: From high resolution seismic point of view. *Journal of Geophysical Research-Solid Earth* 113.
- Domenico, S. N., 1977, elastic properties of unconsolidated porous sand reservoirs: *Geophysics*, 42, 1339-1368.
- Garu, G., Lailly, P., 1993. Sequential migration-aided reflection tomography: an approach to imaging complex structures. *J. Appl. Geophys.* 30, 75-87.
- Gray, S.H., Etgen, J., Dellinger, J., Whitmore, D., 2001. Seismic migration problems and solutions. *Geophysics* 66, 1622-1640.
- Gist, G. A., 1994, interpreting laboratory velocity-measurements in partially gas-saturated rocks: *Geophysics*, 59, 1100-1109.
- Grevemeyer, I., Rosenberger, A., Villinger, H., 2000. Natural gas hydrates on the continental slope off Pakistan: constraints from seismic techniques. *Geophysical Journal International* 140, 295-310.
- Haacke, R.R., Hyndman, R.D., Park, K.P., Yoo, D.G., Stoian, I., Schmidt, U., 2009. Migration and venting of deep gases into the ocean through hydrate-choked chimneys offshore Korea. *Geology* 37, 531-534.
- Haacke, R.R., Westbrook, G.K., Hyndman, R.D., 2007. Gas hydrate, fluid flow and free gas: Formation of the bottom-simulating reflector. *Earth and Planetary Science Letters* 261, 407-420.

- He, T., Spence, G.D., Wood, W.T., Riedel, M., Hyndman, R.D., 2009. Imaging a hydrate-related cold vent offshore Vancouver Island from deep-towed multichannel seismic data. *Geophysics* 74, B23-B36.
- Helgerud, M.B., Dvorkin, J., Nur, A., 2000. Rock physics characterization for gas hydrate reservoirs - Elastic properties, in: Holder, G.D., Bishnoi, P.R. (Eds.), *Gas Hydrates: Challenges for the Future*, pp. 116-125.
- Helgerud, M.B., Dvorkin, J., Nur, A., Sakai, A., Collett, T., 1999. Elastic-wave velocity in marine sediments with gas hydrates: Effective medium modeling. *Geophysical Research Letters* 26, 2021-2024.
- Holbrook, W.S., Hoskins, H., Wood, W.T., Stephen, R.A., Lizarralde, D., 1996. Methane hydrate and free gas on the Blake ridge from vertical seismic profiling. *Science* 273, 1840-1843.
- Hole, J.A., Zelt, B.C., 1995. 3D finite-difference reflection traveltimes. *Geophysical Journal International* 121, 427-434.
- Hornbach, M.J., Holbrook, W.S., Gorman, A.R., Hackwith, K.L., Lizarralde, D., Pecher, I., 2003. Direct seismic detection of methane hydrate on the Blake Ridge. *Geophysics* 68, 92-100.
- Hu, G.W., Ye, Y.G., Zhang, J., Liu, C.L., Diao, S.B., Wang, J.S., 2010. Acoustic properties of gas hydrate-bearing consolidated sediments and experimental testing of elastic velocity models. *Journal of Geophysical Research-Solid Earth* 115.
- Hyndman, R.D., Spence, G.D., 1992. A seismic study of methane hydrate marine bottom simulating reflectors. *Journal of Geophysical Research-Solid Earth* 97, 6683-6698.
- Inamori, T., Hato, M., 2004. Detection of methane hydrate-bearing zones from seismic data. *Resource Geology* 54, 99-104.
- Jaiswal, P., Zelt, C.A., 2008. Unified imaging of multichannel seismic data: Combining traveltime inversion and prestack depth migration. *Geophysics* 73, VE269-VE280.
- Kiyashchenko, D., Plessix, R.-E., Kashtana, B., Troyana, V., 1995. Improved amplitude multi-one-way modeling method. *Wave Motion* 43, 99-115.
- Kopp, H., 2002. BSR occurrence along the Sunda margin: evidence from seismic data. *Earth and Planetary Science Letters* 197, 225-235.
- Kvenvolden, K.A., 1994. Natural Gas Hydrate Occurrence and Issues. *Annals of the New York Academy of Sciences* 715, 236-242.
- Lailly, P., Sinoquet, D., 1996. Smooth velocity models in reflection tomography for imaging complex geological structures. *Geophysical Journal International* 124, 349-362.
- Laird, A.P., Morley, C.K., 2011. Development of gas hydrates in a deep-water anticline based on attribute analysis from three-dimensional seismic data. *Geosphere* 7, 240-259.
- Le Begat, S., Chauris, H., Devaux, V., Nguyen, S., Noble, M., 2004. Velocity model estimation for depth imaging: Comparison of three tomography methods on a 2D real data set. *Geophysical Prospecting* 52, 427-438.

- Lee, M.W., Dillon, W.P., 2001. Amplitude blanking related to the pore-filling of gas hydrate in sediments. *Marine Geophysical Researches* 22, 101-109.
- Lees, J.M., Crosson, R.S., 1989. Tomographic Inversion For 3-Dimensional Velocity Structure At Mount St-Helens Using Earthquake Data. *Journal of Geophysical Research-Solid Earth and Planets* 94, 5716-5728.
- Max, M.D., 2003. *Natural Gas Hydrate in Oceanic and Permafrost Environments*. Kluwer Academic Publishers, AA Dordrecht.
- Müller, C., Bonnemann, C., Neben, S., 2007. AVO study of a gas-hydrate deposit, offshore Costa Rica. *Geophysical Prospecting* 55, 719-735.
- Ojha, M., Sain, K., 2009. Seismic attributes for identifying gas-hydrates and free-gas zones: application to the Makran accretionary prism. *Episodes* 32, 264-270.
- Pasasa, L., Wenzel, F., Zhao, P., 1998. Prestack Kirchhoff depth migration of shallow seismic data. *Geophysics* 63, 1241-1247.
- Powell, C.M., Roots, S.R., Veevers, J.J., 1988. Pre-breakup continental extension in east Gondwanaland and the early opening of the eastern Indian-Ocean. *Tectonophysics* 155, 261-283.
- Riedel, M., Collett, T.S., Kumar, P., Sathe, A.V., Cook, A., 2010. Seismic imaging of a fractured gas hydrate system in the Krishna-Godavari Basin offshore India. *Marine and Petroleum Geology* 27, 1476-1493.
- Rothwell, R.G., Thomson, J., Kahler, G., 1998. Low-sea-level emplacement of a very large Late Pleistocene 'megaturbidite' in the western Mediterranean Sea. *Nature* 392, 377-380.
- Ruan, A.G., Li, J.B., Chu, F.Y., Li, X.Y., 2006. AVO numerical simulation of gas hydrates reflectors beneath seafloor. *Chinese Journal of Geophysics-Chinese Edition* 49, 1826-1835.
- Schneider, W.A., 1978. Integral formulation for migration in two and three dimensions. *Geophysics* 43, 49-76.
- Shipley, T.H., Houston, M.H., Buffler, R.T., Shaub, F.J., McMillen, K.J., Ladd, J.W., Worzel, J.L., 1979. Seismic evidence for widespread possible gas hydrate horizons on continental slopes and rises. *Aapg Bulletin-American Association of Petroleum Geologists* 63, 2204-2213.
- Singh, S.C., Minshull, T.A., 1994. Velocity structure of a gas hydrate reflector at ocean drilling program site-889 from a global seismic wave-form inversion. *Journal of Geophysical Research-Solid Earth* 99, 24221-24233.
- Sloan, E.D., Koh, C., 2007. *Clathrate Hydrates of Natural Gases* 3rd ed. CRC Press.
- Subrahmanyam, C., Chand, S., 2006. Evolution of the passive continental margins of India - a geophysical appraisal. *Gondwana Research* 10, 167-178.

Svensen, H., Planke, S., Malthé-Sorensen, A., Jamtveit, B., Myklebust, R., Eidem, T.R., Rey, S.S., 2004. Release of methane from a volcanic basin as a mechanism for initial Eocene global warming. *Nature* 429, 542-545.

Tinivella, U., Accaino, F., Camerlenghi, A., 2002. Gas hydrate and free gas distribution from inversion of seismic data on the South Shetland margin (Antarctica). *Marine Geophysical Researches* 23, 109-123.

Trehu, A.M., Long, P.E., Torres, M.E., Bohrmann, G., Rack, F.R., Collett, T.S., Goldberg, D.S., Milkov, A.V., Riedel, M., Schultheiss, P., Bangs, N.L., Barr, S.R., Borowski, W.S., Claypool, G.E., Delwiche, M.E., Dickens, G.R., Gracia, E., Guerin, G., Holland, M., Johnson, J.E., Lee, Y.J., Liu, C.S., Su, X., Teichert, B., Tomaru, H., Vanneste, M., Watanabe, M., Weinberger, J.L., 2004. Three-dimensional distribution of gas hydrate beneath southern Hydrate Ridge: constraints from ODP Leg 204. *Earth and Planetary Science Letters* 222, 845-862.

Vidale, J., 1988. Finite-difference travel time calculation. *Bull. Seism. Soc. Am.* 78, 2062-2076.

Versteeg, R.J., 1993. Sensitivity of prestack depth migration to the velocity model. *Geophysics* 58, 873-882.

Wood, W.T., Gettrust, J.F., Chapman, N.R., Spence, G.D., Hyndman, R.D., 2002. Decreased stability of methane hydrates in marine sediments owing to phase-boundary roughness. *Nature* 420, 656-660.

Wood, W.T., Hart, P.E., Hutchinson, D.R., Dutta, N., Snyder, F., Coffin, R.B., Gettrust, J.F., 2008. Gas and gas hydrate distribution around seafloor seeps in Mississippi Canyon, Northern Gulf of Mexico, using multi-resolution seismic imagery. *Marine and Petroleum Geology* 25, 952-959.

Xia, G.Y., Sen, M.K., Stoffa, P.L., 2000. Mapping of elastic properties of gas hydrates in the Carolina trough by waveform inversion. *Geophysics* 65, 735-744.

Yilmaz, O., 2001. *Seismic Data Processing*. Society of Exploration Geophysicists, Tulsa.

Yun, T.S., Santamarina, J.C., Ruppel, C., 2007. Mechanical properties of sand, silt, and clay containing tetrahydrofuran hydrate. *Journal of Geophysical Research-Solid Earth* 112.

Zelt, C.A., 1999. Modelling strategies and model assessment for wide-angle seismic traveltimes data. *Geophysical Journal International* 139, 183-204.

Zelt, C.A., Barton, P.J., 1998. Three-dimensional seismic refraction tomography: A comparison of two methods applied to data from the Faeroe Basin. *Journal of Geophysical Research-Solid Earth* 103, 7187-7210.

Zhao, Q., Guo, J., Hao, S.L., Geng, J.H., 2005. Experiments of physical modeling for petrophysical properties of natural gas hydrate. *Chinese Journal of Geophysics-Chinese Edition* 48, 649-655.

Zillmer, M., Reston, T., Leythaeuser, T., Flueh, E.R., 2005. Imaging and quantification of gas hydrate and free gas at the Storegga slide offshore Norway. *Geophysical Research Letters* 32.

9. Figure captions

Figure 1. Base map. Seismic line used in this study is shown and graduated every 200th CDP. Bathymetry contours are labeled every 50m. Location of sites NGHP-01-10, 12, and 13 with their projection on the seismic line are shown with solid black and white stars respectively. The sites are project along the regional faults, F1 – 4, interpreted after Dewangan *et al.* (2011) in grey dashed lines. Location of the study area with respect to the Indian subcontinent is shown in the inset. Also shown in the inset are the Logging While Drilling (LWD) resistivity from Site NGHP-01-10 and the wireline resistivity from Site NGHP-01-13. Increase in resistivity at both sites compared to a background trend (dashed grey line) suggests presence of hydrates.

Figure 2. Stacked data. (a) Uninterpreted (b) Interpreted. Horizons R1 – R4 used in Unified Imaging are indicated in red. R1 – R4 picks are used for zero offset inversion. Projections of the NGHP-01-10, 12 and 13 wellbores (Figure 3) are overlain. The dashed line is the interpreted BSR. The wedge shape sediment package between R2 and the seafloor indicate that they are syn-tectonic in nature.

Figure 3. Interval velocity model evolution. (a) Vel0 is from the stacking velocity model. (b) Vel1, (c) Vel2, and (d) Vel3 are the evolving velocity models through the cycles in UI. (e) Three possible projections of Sites NGHP-01-10, 12 and 13 are shown in red, blue, and green. The green projection, along the strike of the regional faults (Figure 1), best matches the BSR depth at site NGHP-01-10 and the disconnected nature of hydrates at sites NGHP-01-10 and 12. The resistivity log from NGHP-01-10 is overlaid. Model below R4 has no ray coverage. Velocity contours in km/s are labeled. We assume velocities above 1.7 km/s firmly indicate hydrates and below 1.4 km/s firmly indicate free gas bearing sediments. Solid black lines represent R1 – R4, interpreted on the corresponding depth images (Figure 4). The overlaid white segments are inverted horizons from picks in the stacked data (Figure 2). BSR in (e) is interpreted on the final depth image (Figure 4l). A discrepancy of 10m in BSR depth at NGHP-01-10D in the first projection is indicated in the image.

Figure 4. Depth image evolution. (a) Image0 is migrated using the stacking velocity model Vel0. Subsequent depth migration creating (b) Image1 with Vel1, (c) Image2 with Vel2, and (d) Image3 with Vel3. (e) – (h) are respectively same as (a) – (d) with interpreted horizons R1 (red), R2 (blue), R3 (green), and R4 (yellow) marked with dashed lines. (i) – (l) are same as (a) – (d) with inverted reflection locations corresponding to R1 (red), R2 (blue), R3 (green), and R4 (yellow) overlaid. In (i) – (l), the discrepancy between inverted and interpreted horizons in terms of the congruency factor is indicated. Image3 provides the best congruency and is considered final along with the corresponding velocity model Vel3. In (a) – (d) wedge shape sediment package between R2 and the seafloor indicate that they are syn-tectonic in nature.

Figure 5. Model assessment. a) Difference plot between Vel0 and Vel3. Lateral velocity features unresolved by stacking analysis have been estimated by UI. Inverted arrows indicate CMP location for comparison of migrated gathers before and after UI (Figure 6). (b) Checkerboard test suggests that ray coverage used in UI can resolve features with at least 200m X 100m dimension and 10% maximum

perturbation strength between the seafloor and R4. (c) Comparison of BSR structures in depth images from the three cycles of UI. The difference between BSR from Image0 (from Vel0) and Image3 (from Vel3) is ~15m at the NGHP-01-03 projection location (Figure 3).

Figure 6. Migrated gather comparison. Migrated gather from CDP 640 using (a) Vel0 and (b) Vel3 and from CDP 800 using (c) Vel0 and (d) Vel3 (Figure 5). Improvement in flatness of migrated events such as those indicated by black arrows in (b) and (d) compared to (a) and (c) suggest that the overall update in Vel0 though UI improves the velocity model.

Figure 7. Composite interpretation. (a) Uninterpreted depth image (same as Image3; Figure 4d). NGHP-01-10, 12 and 13 borehole projections (Figure 3) are overlaid. The BSR, indicated by red arrows, is continuous from CMP 200 – 450 and patchy from CMP 500 – 850. (b) Interpreted depth image. Two dominant sets of faults, A and B, are interpreted. The BSR is patchy in fault dominated areas. A possible polygonal fault set is interpreted as dotted lines between CMP 800 – 850. Detailed interpretation of the image within the yellow dashed box is presented in Figure 8(a). (c) Vel3 (Figure 3d) overlay. The seismic blank zone is outlined with a dotted line. Also overlaid are resistivity logs from Sites NGHP-01-10 and 13. BSR is interpreted with a dashed red line. In fault dominated areas, V_P variations more reliably indicate hydrates than the BSR amplitudes. The BSR cannot be identified beyond 900 based on cross-cutting stratigraphy but a possible base of the GHSZ based on the velocity model and the depth image is shown by the dotted red line extending to CMP 1150.

Figure 8. The hydrate – free gas system. (a) Interpretation of the BSR and related faults. The depth image is same as Image3 (Figure 4d). The interpreted BSR is given by a solid red line and the interpreted faults are in dotted lines. BSR between CMP 500 and 850 is patchy. The patchyness is due to interruption by faults. F'1 and F'2 respectively represent small-scale (<5m) sub-seismic scale faults. (b) Cartoon of a diffusive hydrate system. Hydrates are dissipated in fine-grained sediments. The GHSZ is underlain by free gas. (c) Cartoon of mixed diffusive – advective system representative of the hydrate – free gas system interpreted along the seismic line. The previous seafloor and BSR, corresponding to the diffusive system, are labeled and indicated in dashed and dotted lines respectively. The black dashed box corresponds to the seismic image in (a).

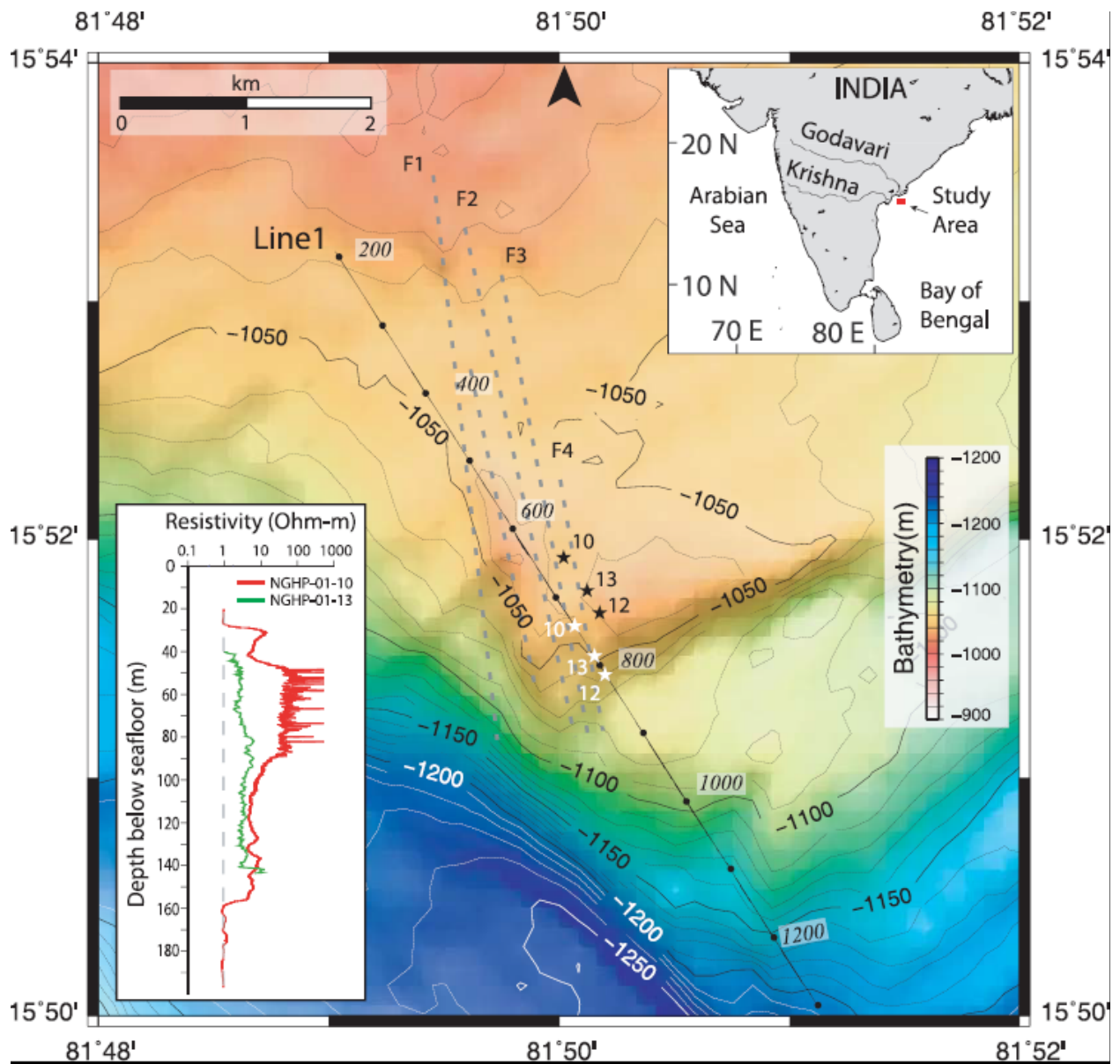


Figure 1

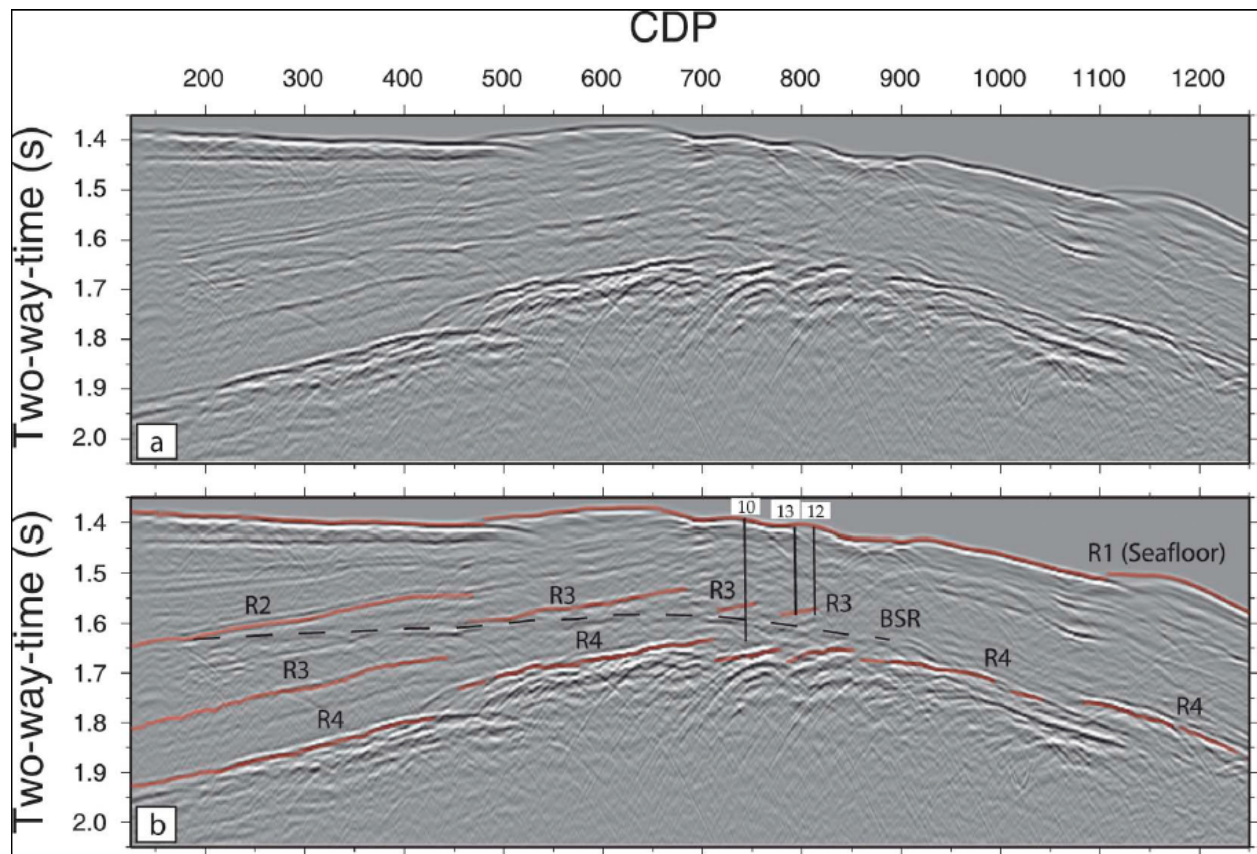


Figure 2

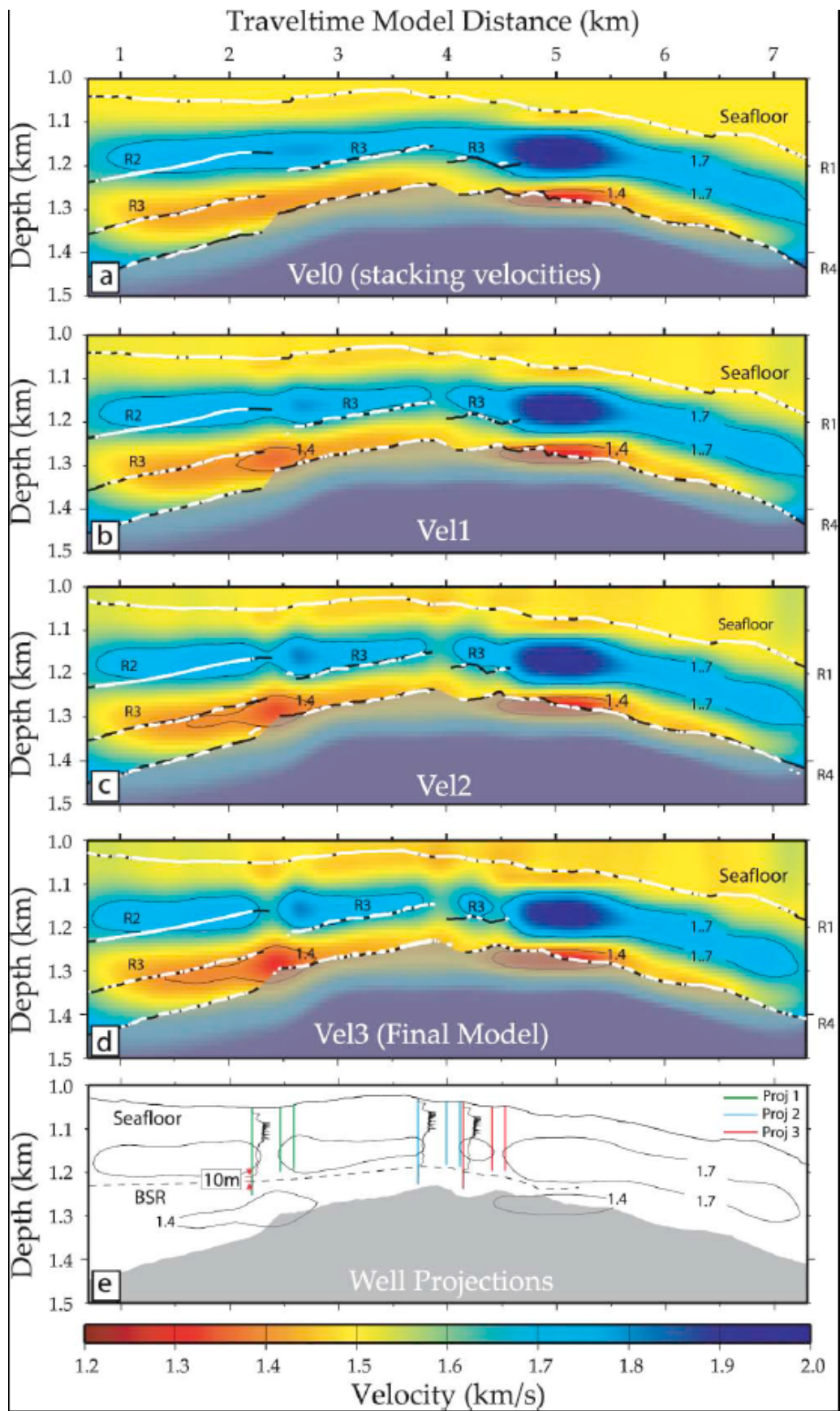


Figure 3

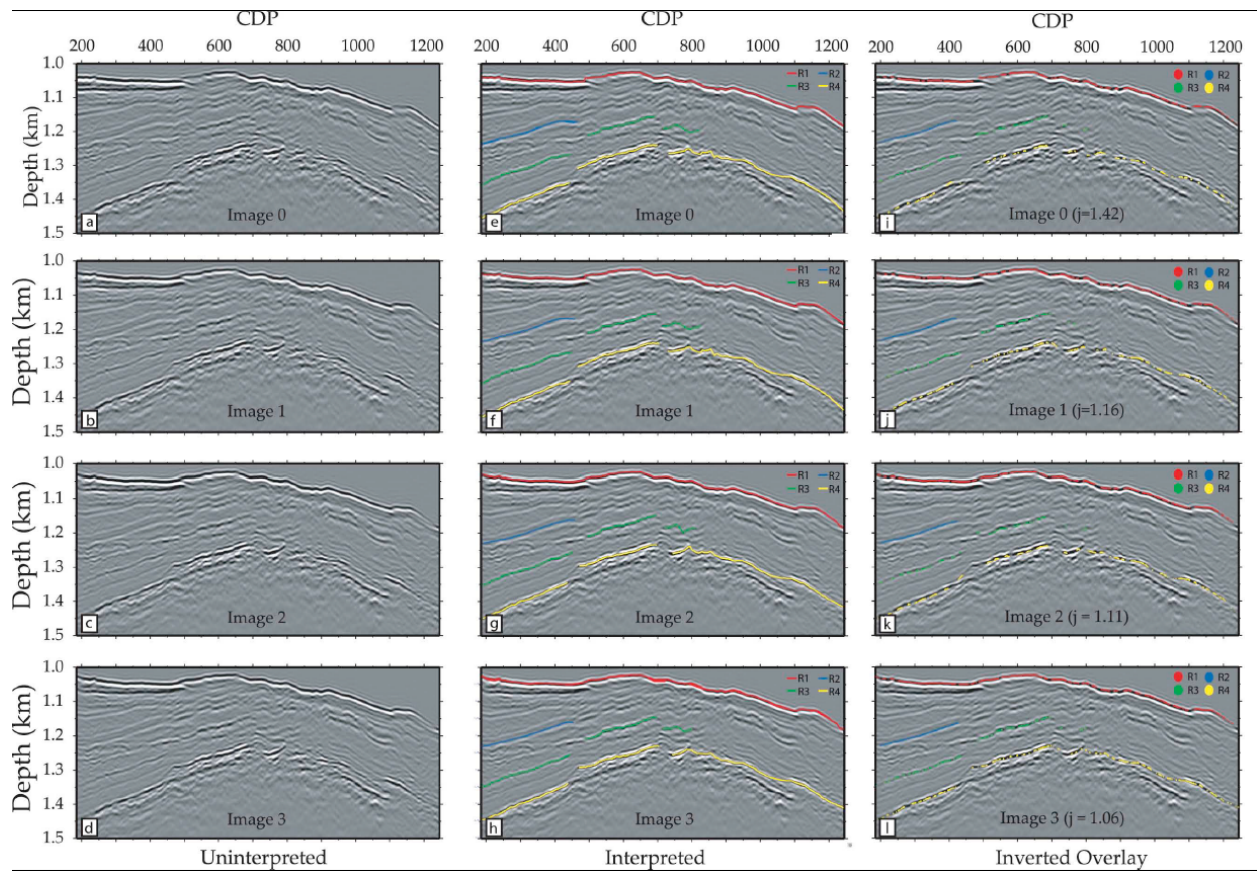


Figure 4

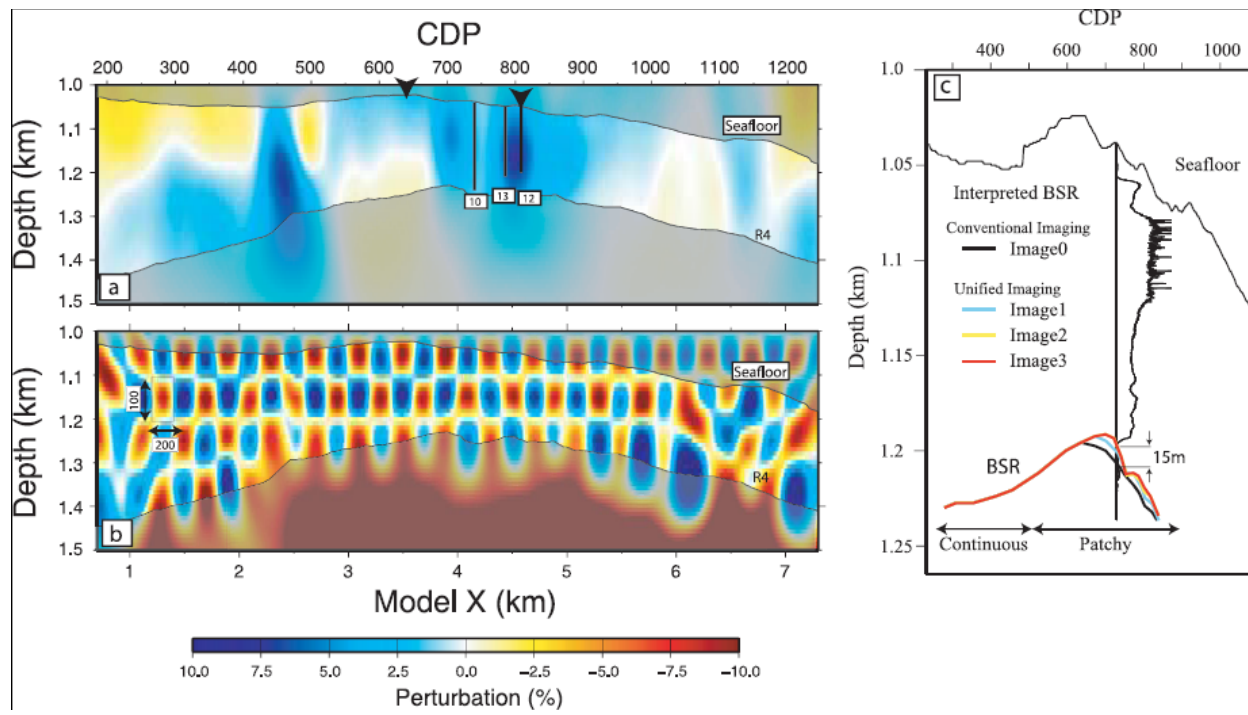


Figure 5

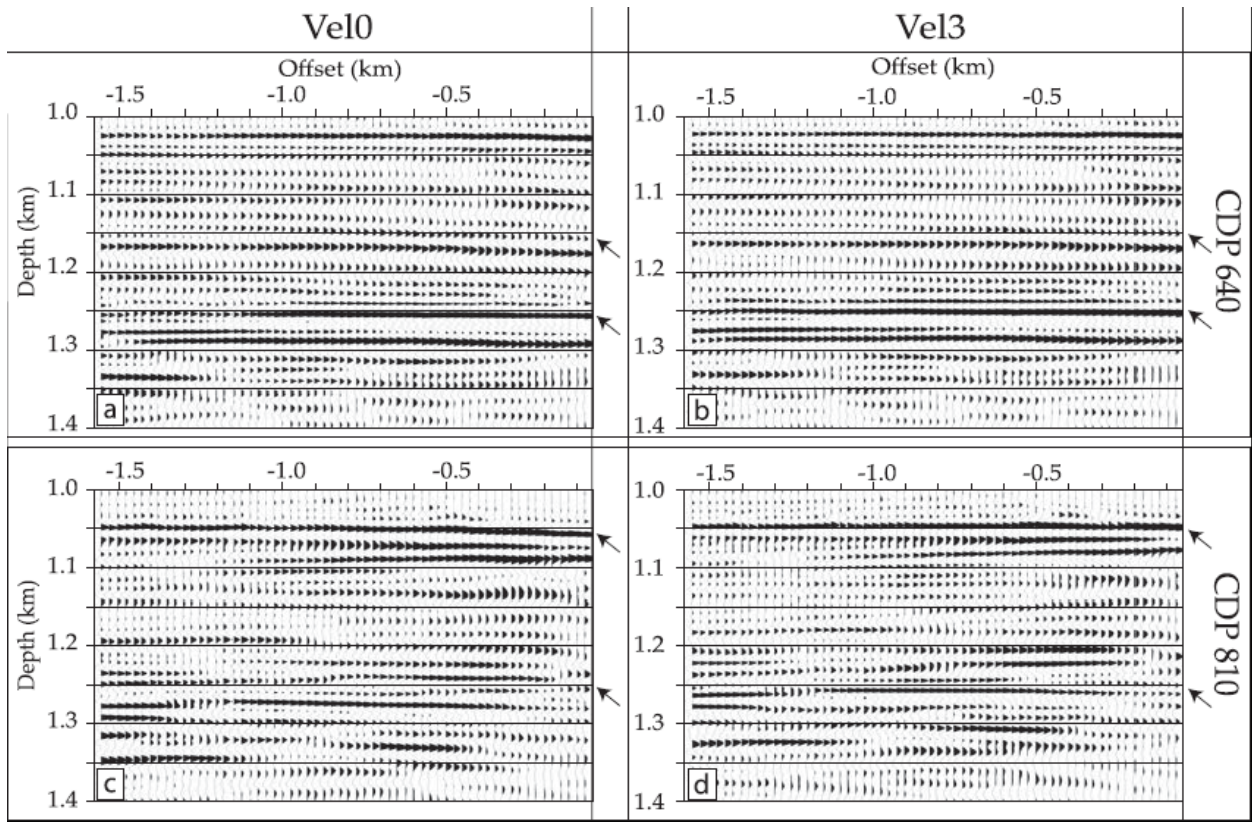


Figure 6

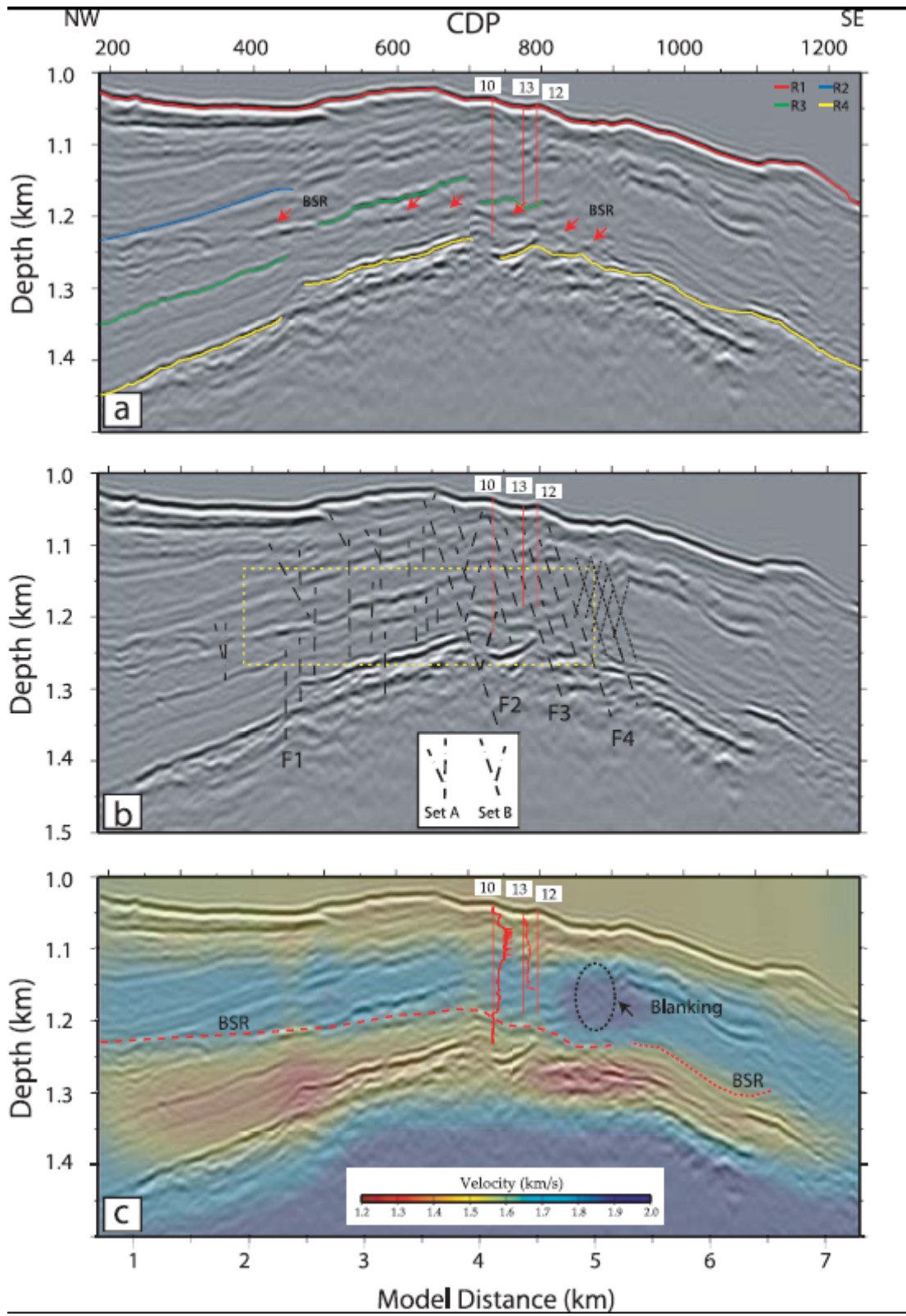


Figure 7

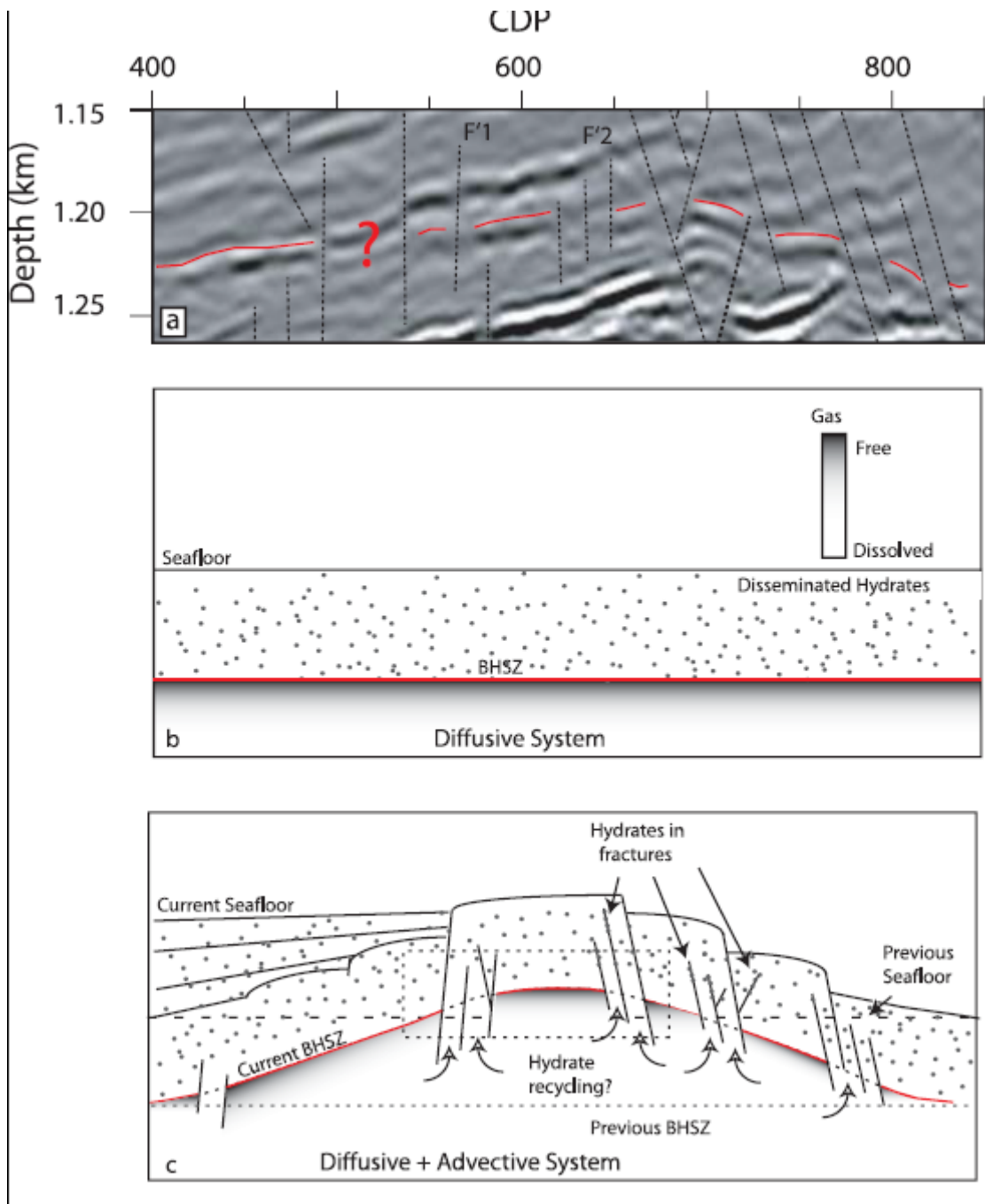


Figure 8